










Experimental quantification of site-specific efficiency of Interatomic Coulombic Decay after inner shell ionization

Catmarna Küstner-Wetekam ^{1✉}, Lutz Marder ¹, Dana Bloß¹, Carolin Honisch¹, Nils Kiefer¹, Clemens Richter^{2,3}, Simon Rubik¹, Rebecca Schaf¹, Christina Zindel ¹, Marko Förstel ⁴, Kirill Gokhberg⁵, André Knie ¹, Uwe Hergenhahn ^{2,3}, Arno Ehresmann ¹, Přemysl Kolorenc ^{6✉} & Andreas Hans ^{1✉}

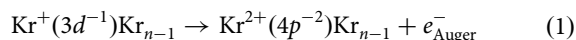
Interatomic Coulombic Decay (ICD) and related interatomic and intermolecular autoionization mechanisms are ubiquitous decay processes of excited atoms and molecules in an environment. It is commonly accepted that the efficiency of ICD of an ionized atom in a cluster increases with an increasing number of nearest neighbors. Here, we present a method for experimental validation of this assumption by a site-specific and quantitative comparison of ICD and its main competitor, Auger decay, in core-level ionized Kr clusters. Our results are in quantitative agreement with scaled theoretical calculations on Kr₂.

¹Universität Kassel, Institut für Physik und CINSaT, Heinrich-Plett-Str. 40, 34132 Kassel, Germany. ²Leibniz-Institut für Oberflächenmodifizierung (IOM), Permoserstr. 15, 04318 Leipzig, Germany. ³Fritz-Haber-Institut der Max-Planck-Gesellschaft, Faradayweg 4-6, 14195 Berlin, Germany. ⁴Technische Universität Berlin, Institut für Optik und Atomare Physik, Hardenbergstr. 36, 10623 Berlin, Germany. ⁵Universität Heidelberg, Physikalisch-Chemisches Institut, Im Neuenheimer Feld 229, 69120 Heidelberg, Germany. ⁶Charles University, Faculty of Mathematics and Physics, Institute of Theoretical Physics, V Holešovičkách 2, 180 00 Prague, Czech Republic. ✉email: c.kuestner-wetekam@uni-kassel.de; premysl.kolorenc@matfyz.cuni.cz; hans@physik.uni-kassel.de

Nonlocal interatomic and intermolecular decay processes are nowadays known to be ubiquitous mechanisms for the relaxation of electronically excited states in dense media. The theoretical prediction of Interatomic Coulombic Decay (ICD) in 1997¹ re-opened a rapidly growing field of experimental and theoretical research^{2–4}. In ICD, the energy stored in an electronic vacancy of an atom is transferred to a remote neighboring atom or molecule, thereby ionizing it. If local auto-ionization is energetically forbidden, ICD may be the only accessible nonradiative relaxation mechanism. ICD has now been studied extensively and proven to occur in van der Waals-bonded (e.g., rare gas gas or molecular clusters) and hydrogen-bonded systems (e.g., water clusters, liquids, and microsolvated biomolecules)⁴. While early experimental work^{5–10} focused on ICD of electronic inner-valence vacancies, the initial states may be prepared in various scenarios, including inner-shell photoionization^{11,12}, (resonant) Auger decay cascades^{13–17}, electron^{18,19} or ion impact²⁰. Also, other energy or charge transfer processes have been identified; for more details, see reviews in refs. 2–4. From early²¹ and more recent²² theoretical works, it has been commonly accepted that the efficiency of ICD increases linearly with the number of nearest neighbors available as decay partners. Although efficiency is a crucial parameter to estimate the importance of all nonlocal processes and their inclusion into models of real-life scenarios, experimental validations of this important and strong assumption using different systems and methods are rare. Only evidence from two experiments has been reported so far: in large Ne clusters, a wider Lorentzian decay width of the 2s photoline (indicating faster decays) was found for the bulk component compared to the surface component⁸. If assumed that the radiative decay width is negligible, which was proven some years later²³, the larger width for the bulk photoelectron peak provides evidence that, indeed, the ICD efficiency is higher for atoms with more neighbors. In water clusters, the ICD efficiency was determined quantitatively as a function of mean cluster size²⁴ and was shown to increase from small to larger clusters. However, in these systems, several factors (nature of the hydrogen bond network, competition between ICD and nuclear dynamics²⁴) complicate an interpretation with respect to the number of nearest neighbors. Also, results for each size were averaged over all sites in the respective clusters. With the purpose of establishing a universal method to quantify the ICD efficiency, we investigate a specific variant of ICD, namely core-level ICD, which was just recently observed in van der Waals clusters¹². In contrast to ICD after inner-valence ionization, core-level ICD is a decay channel of inner-shell vacancies and therefore a competitor of the local Auger decay. Since the Auger decay rate is independent of neighboring atoms, experimental determination of the branching ratio between these competing processes in a single measurement enables us to evaluate the relative efficiency of the ICD process with respect to the Auger decay.

Results

We study the specific case of decay after Kr 3*d* photoionization. Since radiative decay of such shallow core-levels is typically negligible, the dominant relaxation pathway of the 3*d* core vacancy is Auger decay, leading to the well-known MNN-Auger spectrum^{25,26} and leaving one atom of the *n*-atom Kr cluster in a one-site dicationic state with two 4*p* vacancies:



The competing core-level ICD process is sketched in Fig. 1: the transition energy is transferred to a neighboring atom leading to a

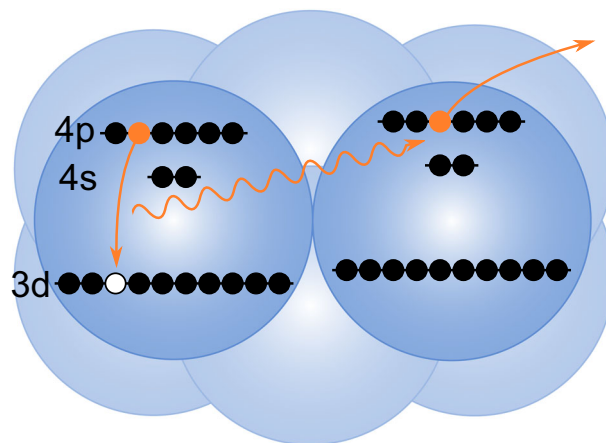
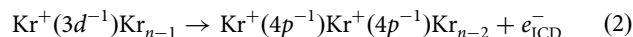


Fig. 1 Schematic representation of core-level ICD in Kr clusters. The black dots represent the electrons occupying the 3*d*, 4*s*, and 4*p* shells in Kr, where fine structure splitting of the orbitals has been neglected for simplicity. The 3*d* core vacancy (depicted as a white dot) is filled by a valence (4*p*, orange dot) electron from the same atom, and the released energy is transferred to the neighboring atom, which is thereby ionized. The ICD electron is shown as an orange dot (4*p* electron), leaving the second Kr atom.

two-site delocalized dicationic state of the cluster:



The number of nearest neighbors of the initially 3*d*-ionized atom and, as we will show, the efficiency of the ICD process depends on the position of the atom in either the bulk or the surface of the cluster. In this experiment, we achieve site sensitivity by coincident detection of the Auger or ICD electron with the respective 3*d* photoelectron. The 3*d* photoelectron shows a spectroscopically measurable difference in binding energies for atoms at different cluster sites, e.g., for atoms on the surface or in the bulk of a cluster, due to differences in screening²⁷.

Experimental results. The high-energy part of the Auger spectrum, attributed to Kr III 4*p*⁻² final state configurations, and the corresponding core-level ICD features, detected in coincidence with the 3*d*_{5/2} fine structure photoelectron component, are shown in Fig. 2a. The 3*d*_{5/2} photoelectron spectrum of Kr, which is presented in Fig. 2b, is well separated into atomic and cluster signal, with the latter being further distinguished into signals originating from surface or bulk atoms, respectively²⁷. The blue and green shaded areas in Fig. 2b indicate ranges of binding energies in which photoemission preferentially occurs from only one of the two types of sites; filtering for electron pairs with a photoelectron falling into one of these intervals is therefore well-suited to establish conditions under which the site-selective Auger and ICD spectra can be observed, presented in Fig. 2a (surface: green solid trace, bulk: blue dashed trace).

Each spectrum in Fig. 2a is normalized to the intensity of the M₅N_{2,3}N_{2,3} Auger electron spectrum with the final configuration of 4*p*⁻² (on the right-hand side of the dashed line), and it is already obvious that the core-level ICD signal originating from bulk atoms has a higher intensity relative to that of the surface atoms. The ICD to Auger decay ratio as a measure of the relative ICD efficiency is obtained by integrating and comparing the signal for both competing processes after background subtraction. To evaluate the ICD efficiency as a function of the average number of neighboring atoms, we determined the branching ratio for electrons in coincidence with photoelectrons with binding

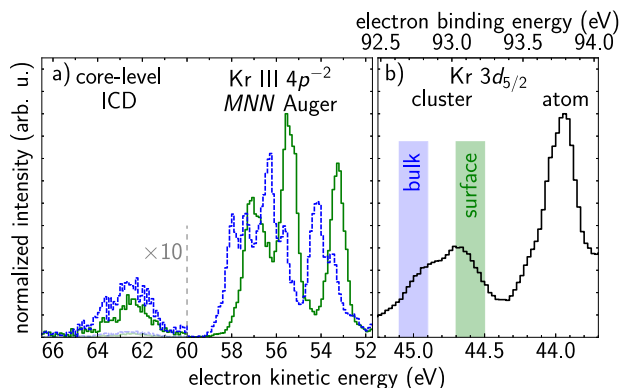


Fig. 2 Coincidental $3d_{5/2}$ photoelectron, Auger and ICD electron spectra.

a High-energy Auger and core-level ICD electrons detected in coincidence with $3d_{5/2}$ photoelectrons from bulk (blue dashed) and surface (green solid) of Kr clusters each normalized to equal area of the $M_5N_{2,3}N_{2,3}$ Auger spectrum between 52.1 and 59.2 eV kinetic energy. **b** Spectrum of the Kr $3d_{5/2}$ photoelectron measured in coincidence with Auger or core-level ICD electrons for atoms and clusters in a partially condensed cluster jet. The cluster signal is additionally split into surface and bulk signals. The blue and green shaded areas indicate the electron kinetic energy ranges used to identify the coincident events shown in **a**.

energies varying in 0.1 eV steps across the photoelectron cluster peaks. The resulting ratios are shown in Fig. 3.

We observe a significant increase in the core-level ICD efficiency during the transition from atoms located at the surface to those located in the bulk. This is directly correlated to the number of nearest neighbors, which increases from 6 (corner) to 12 (bulk) atoms. Note that due to the intrinsic width of the states²⁷, we cannot resolve different surface states corresponding to corner, edge, and face atoms. We observe, however, an increasing ICD branching ratio for surface atoms with lower binding energies, which is a strong indication that indeed different surface sites contribute to the signal in this range.

Theoretical calculations. For a better quantitative evaluation of the experimental ICD branching ratios, we performed theoretical calculations of the expected value in Kr_2 dimers. As in ref. 22, we have employed the non-relativistic Fano-ADC(2)x-Stieltjes method²⁸ to compute total and partial decay rates of the $3d$ vacancy in Kr_2 dimers. The partial rates were determined through operators P_β , projecting on individual decay channels within the final states configuration space as described in refs. 29,30. The calculations were performed using the cc-pwCV5Z-PP basis set, in which the scalar relativistic effects are taken into account via a 10-electron effective core potential (ECP). To better represent the continuum, the basis was further augmented by $5s$, $5p$, $5d$, and $5f$ continuum-like Gaussian functions³¹. For further details, see the supplementary material in ref. 22. At the equilibrium interatomic distance $R_{eq} = 4.0$ Å of the Kr_2 dimer, the total calculated ICD probability is $(0.09 \pm 0.01)\%$. However, if only the $4p^{-2}$ one-site Auger decay channels are taken into account, as in the present experiment, the ICD probability increases to $(0.13 \pm 0.01)\%$ per neighboring atom. Based on the icosahedral structure of the cluster²⁷, this results in an ICD to Auger decay branching ratio of $(0.78 \pm 0.06)\%$ for corner atoms to $(1.56 \pm 0.12)\%$ for bulk atoms. The calculations reproduce the experimental values of $(0.63 \pm 0.12)\%$ to $(2.07 \pm 0.20)\%$ reasonably, except for an underestimation for bulk atoms. We expect this discrepancy to originate mainly from two contributions which are not considered in the theoretical model. First, ICD with next-nearest neighbors may contribute stronger for bulk than for surface

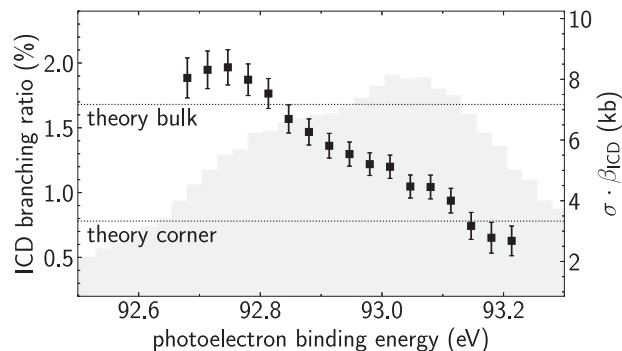


Fig. 3 Cluster-site dependent ICD branching ratio. The left y-axis shows the ICD branching ratio in percent (black squares), i.e., the ICD electron intensity normalized to the total intensity of ICD and Auger electron signals as a function of the photoelectron binding energy, and the right y-axis shows the corresponding absolute scale given by the product of the absolute photoionization cross section σ and the ICD branching ratio β_{ICD} . The error bar shows the statistical error for the branching ratio; the error for the absolute scale is not shown due to unknown uncertainties from used literature values. The two black dotted lines indicate the theoretically calculated values for the ICD branching ratio of bulk and corner atoms. The corresponding photoelectron spectrum is shown in the background (gray shaded area).

atoms, as the contribution is non-negligible³². Second, the average interatomic distance is somewhat smaller for bulk atoms, resulting in a higher ICD decay rate.

To support this conjecture, we have evaluated the $4p^{-2}$ ICD to Auger decay branching ratio as a function of the interatomic distance in the dimer, see Fig. 4. In the region around 4.0 Å, the experimental value for the bulk atoms can be reproduced by assuming the internuclear distance in the bulk to be shortened to about 3.93 Å, which seems entirely plausible.

Finally, we mention that relativistic effects might play a role. Indeed, according to the full four-component description of the Auger decay in a Kr atom, they might account for as much as 20% of the decay rate³³. However, recent more accurate Fano-ADC(2,2) calculations³⁴ suggest that the non-relativistic theory with scalar relativistic effects accounted for through ECP can fully reproduce the experimental Auger rates if double Auger decay channels are included. Since these channels are filtered out in the present coincidence experiment, the Fano-ADC(2)x method combined with ECP is the appropriate method for its interpretation.

ICD probability on an absolute scale. Using atomic reference data, we can determine the ICD probability on an absolute scale. The absolute photoionization cross section of Kr $3d$ of 3.35 Mb at 137.5 eV photon energy³⁵ and the intensity ratio of $3d_{5/2}$ to $3d_{3/2}$ of 1.45²⁶ yields the absolute Kr $3d_{5/2}$ photoionization cross section of $\sigma = 1.98$ Mb. The atomic branching ratios of the Auger decay following $3d_{5/2}$ photoionization²⁶ were then used to obtain the branching ratio of Auger decays into $4p^{-2}$ final states as $\beta_{Auger} = 21.5\%$. Multiplication of this value with the ICD branching ratio (black dots shown in Fig. 3) yields the site-specific ICD branching ratio β_{ICD} , with respect to the initial photoionization. Finally, the core-level ICD probability can be put on an absolute scale by multiplication of the absolute photoionization cross section σ and the branching ratio β_{ICD} , the result of which is depicted in Fig. 3 (right y-axis). The calculated ICD probability $\sigma \cdot \beta_{ICD}$ must be multiplied by the total uncertainty of the used literature values, namely the $3d$ photoionization cross section, the $3d_{5/2}$ to $3d_{3/2}$ ratio, and the Auger decay branching

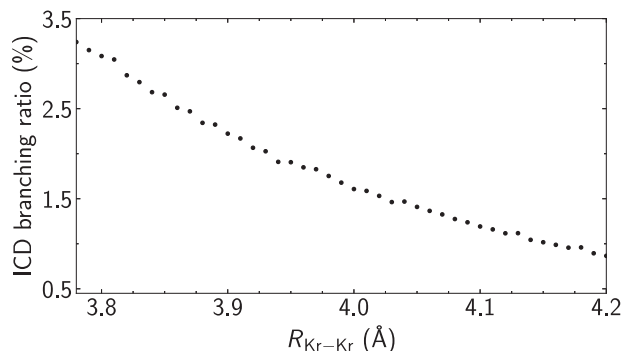


Fig. 4 Computed ICD branching ratio. ICD branching ratio as a function of the internuclear distance R of Kr atoms in a dimer scaled linearly with the number of nearest neighbors (12 atoms) for bulk atoms in an icosahedral arrangement, calculated using the Fano-ADC(2)x (extended second-order algebraic diagrammatic construction) method.

ratio into $4p^{-2}$ final states and the statistical error shown in Fig. 3. But the uncertainties of the literature values are unavailable. Additionally, we assume that the atomic quantities are valid for clusters.

Conclusion

In conclusion, we experimentally quantified the dependency of ICD rates on the number of nearest neighbors by measuring the ratio of ICD events to the competing Auger decay using electron–electron coincidence spectroscopy. The obtained ICD efficiency of up to $(2.07 \pm 0.20)\%$ is in good agreement with our theoretical calculations. Due to overlapping states of different surface sites, a linear dependence cannot be confirmed unambiguously. Good agreement between theory and experiment suggests, however, that except for a slight underestimation of bulk values, state-of-the-art theory explains the reality satisfactorily. Additionally, we estimated absolute ICD cross sections using atomic reference data. We emphasize that the experimental method we present is universal as long as local and nonlocal decay can be spectroscopically separated. This makes it potentially applicable to more complex systems, e.g., molecular clusters or liquids, in which quantification of ICD efficiencies is still lacking.

Methods

Experimental technique. The experiment was performed at the Helmholtz-Zentrum Berlin (BESSY II) using synchrotron radiation at the UE56-2 PGM-2 beamline³⁶. The experimental set-up for electron–electron coincidence spectroscopy consists of a magnetic bottle type time-of-flight electron spectrometer³⁷ and a cryogenic cluster source cooled by a liquid N_2 cryostat. The cluster jet was produced by the supersonic expansion of gaseous Kr through an 80 μm conical copper nozzle (30° full opening angle) cooled to $T = 130$ K and with a back pressure of $p = 540$ mbar. It passed a 1-mm skimmer before crossing the monochromatic synchrotron radiation. Note that under these experimental conditions, the target jet will contain both clusters and uncondensed atoms. Using empirical scaling laws³⁸, the mean size of the clusters is estimated to be $\langle N \rangle = 177$ atoms. At 137.5 eV exciting-photon energy, a -39 V retardation potential was applied to the electron drift tube to resolve individual channels of the Auger electron spectrum.

Data acquisition and evaluation. The presented data has been recorded over 102 min and contains 1.1 million events of electron–electron coincidences. These events were measured in time intervals of two consecutive synchrotron pulses (circulation time between two pulses: 800 ns) to estimate the number of accidental coincidences and eliminate these from the measured data.

In Fig. 2b, the obtained photoelectron spectrum is shown in the form of a histogram of all measured events within the given kinetic energy interval. The time-of-flight data is calibrated to kinetic energies using the well-known atomic $M_5N_{2,3}N_{2,3}$ Auger electron features²⁶. The spectra of true coincidental events in energy ranges assigned to photoelectrons from cluster surface or bulk sites, as indicated by the shaded areas in Fig. 2b, are depicted in Fig. 2a and show the corresponding Kr $M_5N_{2,3}N_{2,3}$ Auger and core-level ICD spectra.

To obtain the ICD branching ratios (see Fig. 3), we used a sequence of 0.1 eV-wide filters across the cluster photoelectron spectrum and determined the coincidentally measured Auger and ICD electron spectra for each slice. After background subtraction, we integrated the Auger (I_{Auger}) and ICD (I_{ICD}) signals, respectively, and thus calculated the ICD branching ratio $\beta_{\text{ICD}} = \frac{I_{\text{ICD}}}{I_{\text{Auger}} + I_{\text{ICD}}}$.

Computational method. The partial ICD and Auger decay widths were computed using the Fano-ADC-Stieltjes method^{28,34}. This method relies on the Fano–Feshbach theory³⁹, according to which a resonance state is composed of a bound $|\Phi\rangle$ and continuum $|\chi_{\beta, \epsilon_\beta}\rangle$ components, where the continuum component describes the motion of the free electron of energy ϵ_β in the open channel β . The partial decay width associated with a specific channel is given as

$$\Gamma_\beta = 2\pi \left| \langle \Phi | \hat{H} - E_r | \chi_{\beta, \epsilon_\beta} \rangle \right|^2 \quad (3)$$

where $E_r \approx \langle \Phi | \hat{H} | \Phi \rangle$ is the real part of the resonance energy. The total width is obtained from Eq. (3) by summing over all open channels.

To represent the required multielectron wave functions, we employed the ADC(2)x method for the Green's function in the intermediate state representation⁴⁰. It allows to separate the electronic configuration space into the subspace Q , containing the bound components, and the subspace P of the final continuum states. The channel projectors P_β were constructed using the generalized localization procedure as described in ref. 29. The subspace of the closed channels is then defined as $Q = 1 - \sum_\beta P_\beta$. The Diagonalization of the projected electronic Hamiltonians, QH_Q and PH_P , provides $|\Phi\rangle$ and $|\chi_{\beta, \epsilon_\beta}\rangle$. Since square-integrable Gaussian type functions were used as the basis set in the calculations, we employed the Stieltjes imaging technique^{41,42} for proper normalization of the continuum component.

The calculations were performed using the cc-pwCV5Z-PP basis set, accounting for the scalar relativistic effect via a 10-electron effective core potential. For an improved representation of the continuum electronic states, the basis was augmented by 5s-type, 5p-type, 5d-type, and 5f-type Kaufmann–Baumeister–Jungen continuum-like functions³¹ (for further details, see the supplementary material of ref. 22). Restricted Hartree–Fock reference state and the two-electron integrals required by the ADC methodology were obtained using MOLCAS quantum chemistry package⁴³.

Data availability

Data shown in this study are available from the corresponding authors (A.H., C.K., and P.K.) upon reasonable request.

Code availability

The code used in this study is available from the corresponding authors (A.H., C.K., and P.K.) upon reasonable request.

Received: 17 June 2022; Accepted: 3 March 2023;

Published online: 17 March 2023

References

- Cederbaum, L. S., Zobeley, J. & Tarantelli, F. Giant intermolecular decay and fragmentation of clusters. *Phys. Rev. Lett.* **79**, 4478 (1997).
- Hergenbahn, U. Interatomic and intermolecular coulombic decay: the early years. *J. Electron Spectros. Relat. Phenomena* **184**, 78 (2011).
- Jahnke, T. Interatomic and intermolecular Coulombic decay: the coming of age story. *J. Phys. B: At. Mol. Opt. Phys.* **48**, 082001 (2015).
- Jahnke, T. et al. Interatomic and intermolecular Coulombic decay. *Chem. Rev.* **120**, 11295 (2020).
- Thissen, R., Lablanquie, P., Hall, R. I., Ukai, M. & Ito, K. Photoionization of argon, krypton and xenon clusters in the inner valence shell region. *Eur. Phys. J. D* **4**, 335–342 (1998).
- Marburger, S., Kugeler, O., Hergenbahn, U. & Möller, T. Experimental evidence for interatomic Coulombic decay in Ne clusters. *Phys. Rev. Lett.* **90**, 203401 (2003).
- Jahnke, T. et al. Experimental observation of interatomic Coulombic decay in neon dimers. *Phys. Rev. Lett.* **93**, 163401 (2004).
- Öhrwall, G. et al. Femtosecond interatomic Coulombic decay in free neon clusters: large lifetime differences between surface and bulk. *Phys. Rev. Lett.* **93**, 173401 (2004).
- Lablanquie, P. et al. Appearance of interatomic Coulombic decay in Ar, Kr, and Xe homonuclear dimers. *J. Chem. Phys.* **127**, 154323 (2007).
- Liu, X.-J. et al. Evidence of sequential interatomic decay in argon trimers obtained by electron–triple-ion coincidence spectroscopy. *J. Phys. B: At. Mol. Opt. Phys.* **40**, F1 (2007).

11. Thürmer, S. et al. On the nature and origin of dicationic, charge-separated species formed in liquid water on X-ray irradiation. *Nat. Chem.* **5**, 590 (2013).
12. Hans, A. et al. Core-level interatomic Coulombic decay in van der Waals clusters. *Phys. Rev. Res.* **2**, 012022 (2020).
13. Aoto, T. et al. Properties of resonant interatomic Coulombic decay in Ne dimers. *Phys. Rev. Lett.* **97**, 243401 (2006).
14. Morishita, Y. et al. Experimental evidence of interatomic Coulombic decay from the Auger final states in argon dimers. *Phys. Rev. Lett.* **96**, 243402 (2006).
15. Kreidi, K. et al. Relaxation processes following 1s photoionization and Auger decay in Ne₂. *Phys. Rev. A* **78**, 043422 (2008).
16. Kimura, M. et al. Controlling low-energy electron emission via resonant-Auger-induced interatomic Coulombic decay. *J. Phys. Chem. Lett.* **4**, 1838 (2013).
17. Trinter, F. et al. Resonant Auger decay driving intermolecular Coulombic decay in molecular dimers. *Nature* **505**, 664 (2014).
18. Ren, X., Jabbour Al Maalouf, E., Dorn, A. & Denifl, S. Direct evidence of two interatomic relaxation mechanisms in argon dimers ionized by electron impact. *Nat. Commun.* **7**, 11093 (2016).
19. Yan, S. et al. Interatomic relaxation processes induced in neon dimers by electron-impact ionization. *Phys. Rev. A* **97**, 010701(R) (2018).
20. Kim, H.-K. et al. Ion-impact-induced interatomic Coulombic decay in neon and argon dimers. *Phys. Rev. A* **88**, 042707 (2013).
21. Santra, R., Zobeley, J. & Cederbaum, L. Electronic decay of valence holes in clusters and condensed matter. *Phys. Rev. B* **64**, 245104 (2001).
22. Liu, L., Kolorenč, P. & Gokhberg, K. Efficiency of core-level interatomic Coulombic decay in rare-gas dimers. *Phys. Rev. A* **101**, 033402 (2020).
23. Förstel, M., Arion, T. & Hergenhanh, U. Measuring the efficiency of interatomic coulombic decay in Ne clusters. *J. Electron Spectros. Relat. Phenomena* **191**, 16 (2013).
24. Richter, C. et al. Competition between proton transfer and intermolecular Coulombic decay in water. *Nat. Commun.* **9**, 4988 (2018).
25. Werme, L. O., Bergmark, T. & Siegbahn, K. The high resolution L_{2,3} MM and M_{4,5} NN Auger spectra from krypton and M_{4,5} NN and N_{4,5} OO Auger spectra from xenon. *Phys. Scr.* **6**, 141 (1972).
26. Palaudoux, J. et al. Multielectron spectroscopy: Auger decays of the krypton 3d hole. *Phys. Rev. A* **82**, 043419 (2010).
27. Hatsui, T. et al. Photoionization of small krypton clusters in the Kr 3d regime: evidence for site-specific photoemission. *J. Chem. Phys.* **123**, 154304 (2005).
28. Averbukh, V. & Cederbaum, L. S. Ab initio calculation of interatomic decay rates by a combination of the Fano ansatz, Green's-function methods, and the Stieltjes imaging technique. *J. Chem. Phys.* **123**, 204107 (2005).
29. Stumpf, V., Scheit, S., Kolorenč, P. & Gokhberg, K. Electron transfer mediated decay in NeXe triggered by K-LL Auger decay of Ne. *Chem. Phys.* **482**, 192 (2017).
30. Kolorenč, P. & Sisourat, N. Interatomic Coulombic decay widths of helium trimer: ab initio calculations. *J. Chem. Phys.* **143**, 224310 (2015).
31. Kaufmann, K., Baumeister, W. & Jungen, M. Universal Gaussian basis sets for an optimum representation of Rydberg and continuum wavefunctions. *J. Phys. B: At. Mol. Opt. Phys.* **22**, 2223 (1989).
32. Fasshauer, E. Non-nearest neighbour ICD in clusters. *New J. Phys.* **18**, 043028 (2016).
33. Fasshauer, E., Kolorenč, P. & Pernpointner, M. Relativistic decay widths of autoionization processes: the relativistic FanoADC-Stieltjes method. *J. Chem. Phys.* **142**, 144106 (2015).
34. Kolorenč, P. & Averbukh, V. Fano-ADC(2,2) method for electronic decay rates. *J. Chem. Phys.* **152**, 214107 (2020).
35. Aksela, S., Aksela, H., Levasalmi, M., Tan, K. H. & Bancroft, G. M. Partial photoionization cross sections of Kr 3d, 4s, and 4p levels in the photon energy range 37–160 eV. *Phys. Rev. A* **36**, 3449 (1987).
36. Weiss, M. R. et al. The elliptically polarized undulator beamlines at BESSY II. *Nucl. Instrum. Methods Phys. Res. A* **468**, 449–452 (2001).
37. Mucke, M. et al. Performance of a short “magnetic bottle” electron spectrometer. *Rev. Sci. Instrum.* **83**, 063106 (2012).
38. Buck, U. & Krohne, R. Cluster size determination from diffractive He atom scattering. *J. Chem. Phys.* **105**, 5408 (1996).
39. Fano, U. Effects of configuration interaction on intensities and phase shifts. *Phys. Rev.* **124**, 1866 (1961).
40. Mertins, F. & Schirmer, J. Algebraic propagator approaches and intermediate-state representations. I. The biorthogonal and unitary coupled-cluster methods. *Phys. Rev. A* **53**, 2140 (1996).
41. Müller-Plathe, F. & Diercksen, G. H. F. Perturbative-polarization-propagator study of the photoionization cross section of the water molecule. *Phys. Rev. A* **40**, 696 (1989).
42. Hazi, A. U. A purely L2 method for calculating resonance widths. *J. Phys. B* **11**, L259 (1978).
43. Aquilante, F. et al. MOLCAS 7: the next generation. *J. Comput. Chem.* **31**, 224–247 (2010).

Acknowledgements

We thank HZB for beamtime allocation and the BESSY II staff for assistance. This work was supported by the Deutsche Forschungsgemeinschaft (DFG) (Project No. 328961117—SFB 1319 ELCH and Research Unit FOR 1789) and the German Federal Ministry of Education and Research (BMBF) (Project 05K19RK2). P.K. acknowledges financial support from the Czech Science Foundation (Project GACR No. 22-22658S).

Author contributions

A.H., A.K., and U.H. conceived the experiment. A.K., C.R., and M.F. prepared the experiment. A.H., C.K., and L.M. performed the experiment with the assistance of C.H., C.Z., D.B., N.K., R.S., and S.R.; C.K. did the data evaluation with the help of L.M. and the supervision of A.E. and A.H.; P.K. performed the theoretical calculations with the support of K.G.; C.K. and P.K. wrote the article with the support of A.E., A.H., and U.H.; All authors reviewed the results and approved the final version of this article.

Funding

Open Access funding enabled and organized by Projekt DEAL.

Competing interests

The authors declare no competing interests.

Additional information

Correspondence and requests for materials should be addressed to Catmarna Küstner-Wetekam, Přemysl Kolorenč or Andreas Hans.

Peer review information *Communications Physics* thanks Pascal Lablanquie and the other, anonymous, reviewer(s) for their contribution to the peer review of this work.

Reprints and permission information is available at <http://www.nature.com/reprints>

Publisher's note Springer Nature remains neutral with regard to jurisdictional claims in published maps and institutional affiliations.



Open Access This article is licensed under a Creative Commons Attribution 4.0 International License, which permits use, sharing, adaptation, distribution and reproduction in any medium or format, as long as you give appropriate credit to the original author(s) and the source, provide a link to the Creative Commons license, and indicate if changes were made. The images or other third party material in this article are included in the article's Creative Commons license, unless indicated otherwise in a credit line to the material. If material is not included in the article's Creative Commons license and your intended use is not permitted by statutory regulation or exceeds the permitted use, you will need to obtain permission directly from the copyright holder. To view a copy of this license, visit <http://creativecommons.org/licenses/by/4.0/>.

© The Author(s) 2023